Magneto-hydrodynamical nonlinear simulations of magnetically confined plasmas using Smooth Particle Hydrodynamics (SPH)

L. Vela Vela,[1, a)] R. Sanchez,[1] J.M. Reynolds-Barredo,[1] and J. Geiger[2]
[1)] *Departamento de Física, Universidad Carlos III de Madrid, Leganés, Spain.*
[2)] *Max-Planck Institute for Plasma Physics, Greifswald, Germany.*

(Dated: 12 January 2019)

The successful application of techniques inspired in Smoothed Particle Hydrodynamics (SPH) to magnetohydrodynamical (MHD) nonlinear simulations of magnetically confined plasmas requires the previous solution to a number of challenging issues that are still not fully resolved. Namely, the construction of precise, arbitrary initial conditions in complicated geometries, the formulation of adequate boundary conditions for the magnetic field and the correct treatment of three-dimensional toroidal boundaries of arbitrary shape. In this paper we present an SPH implementation of the nonlinear MHD equations that includes our proposed solution to these issues and test its performance on a broad selection of nonlinear MHD problems: 1) The propagation of circularly-polarized Alfvén waves; 2) The occurrence of magnetic reconnection for a Harris current-sheet and 3) The nonlinear MHD stability properties of various cylindrical pinches.

Keywords: SPH, SPMHD, ideal MHD, resistive MHD, nonlinear simulations

I. INTRODUCTION

Smoothed Particle Hydrodynamics (SPH) was first introduced in the late 70's by Gingold and Monaghan[1] together with Lucy[2] as a Lagrangian numerical method to solve the equations of hydrodynamics[3]. Since then, the method has gained both popularity and robustness[4] and has been successfully extended to simulate a wide variety of MHD scenarios[5], mostly in the realm of astrophysical plasmas[6]. In SPH, the particles serve as interpolation nodes where any field of interest (density, velocity, magnetic field, etc) can be easily found from the set of values associated to each neighbouring particle. This interpolation permits the discretisation of the spatial derivatives of the equations of MHD on a co-moving frame to obtain evolution equations for each physical field. The fact that in SPH all the fields are "carried by the particles" means that no structured mesh is needed, which in principle endows the method with the theoretical capability of easily handling complex boundary shapes, treating free-boundary stability problems, and giving it a great potential for an efficient parallelisation.

Although magnetically confined plasmas (MCP) and astrophysical plasmas are described by very similar equations, SPH techniques have only been applied to the latter to the best of our knowledge. The main reason is probably that astrophysical plasmas can be often considered boundless (using, for instance, periodic boundary conditions) so that no treatment of the boundary is needed. This is certainly not the case for MCPs, that are usually confined within a vacuum vessel and limited by either a limiter or a divertor.

The main issues that need to be addressed, in our opinion, to make possible the SPH simulation of MCPs in the context of nonlinear MHD are: 1) The capability of constructing arbitrarily complex initial conditions with density profiles that may not have any exploitable symmetries and that have very low particle noise; 2) The consistent treatment of ghost-particles to enforce boundary conditions in the presence of curved boundaries, some of which can become incredibly convoluted in toroidal configurations as seen in modern stellarators and 3) The formulation of boundary conditions for the magnetic field in the presence of conducting walls. We have recently proposed solutions to the first two of these issues[7,8]. In the present paper we proceed to address the third one and include all of them in a novel SPH implementation of the full nonlinear MHD equations that should have all the needed elements to enable the future realization of MCP nonlinear MHD simulations. Our SPH implementation is then illustrated and tested on a battery of nonlinear MHD simulations that encompass dynamics as varied as Alfén wave propagation, magnetic reconnection and cylindrical pinch stability.

The article is organised as follows: Chap. II introduces the SPH method and the set of equations used in the nonlinear simulation of MHD systems. Chap. III describes in detail the solutions to the three aforementioned challenging issues. Chap. IV tests our SPH implementation against a battery of problems that evaluate its ability to simulate nonlinear, ideal and resistive, MHD dynamics. Finally, conclusions and future avenues of work are discussed in Chap. V.

II. SMOOTHED PARTICLE HYDRODYNAMICS

A. Continuum Equations

As a numerical method, SPH was originally designed to solve the equations of hydrodynamics but the method was soon extended to include the equations of magneto-

[a)] Electronic mail: luvelav@fis.uc3m.es

hydrodynamics in its ideal[3], resistive[9], visco-resistive, ambipolar and Hall versions[6]. Here we will limit ourselves to the resistive-MHD model whose equations, in continuum form, are:

$$\frac{\mathrm{d}\rho}{\mathrm{d}t} = -\rho(\nabla\cdot\mathbf{v}) \tag{1}$$

$$\rho\frac{\mathrm{d}\mathbf{v}}{\mathrm{d}t} = \nabla\cdot\mathcal{S} \tag{2}$$

$$\frac{\mathrm{d}\mathbf{B}}{\mathrm{d}t} = (\mathbf{B}\cdot\nabla)\,\mathbf{v} - \mathbf{B}(\nabla\cdot\mathbf{v}) + \nabla\cdot\mathcal{F} \tag{3}$$

$$\rho\frac{\mathrm{d}u}{\mathrm{d}t} = -p(\nabla\cdot\mathbf{v}) + \eta J^2 \tag{4}$$

where $\mathrm{d}/\mathrm{d}t = \partial/\partial t + \mathbf{v}\cdot\nabla$ and the variables $\rho, \mathbf{v}, \mathbf{B}, \mathbf{J}$ and u respectively represent the mass density, velocity, magnetic field, current density and thermal energy. The tensors $\mathcal{S}$ and $\mathcal{F}$ are given by:

$$\mathcal{S} = -\left(p + \frac{B^2}{2\mu_0}\right)\mathbb{I} + \frac{\mathbf{B}\otimes\mathbf{B}}{\mu_0} \tag{5}$$

where $\otimes$ is the tensor products between two vectors, and

$$\mathcal{F} = \eta\left(\nabla\mathbf{B}^T - \nabla\mathbf{B}\right) \tag{6}$$

where the superscript ^{T} stands for transpose operator and η is the resistivity of the system that may vary in space. The thermodynamic pressure p is related to the other variables via the equation of state for ideal gases:

$$p = (\gamma - 1)u\rho \tag{7}$$

with γ being the specific heat ratio. The current density is related to the magnetic field via Ampere's Law:

$$\mu_0\mathbf{J} = \nabla\times\mathbf{B} \tag{8}$$

For finite resistivity, dissipation of the magnetic field takes place via the tensor $\mathcal{F}$, which is a generalisation of the well-known expression $\eta\nabla^2\mathbf{B}$ for variable resistivity, whilst Ohmic-heating happens in the thermal energy equation via the term $\propto \eta J^2$.

B. The mass density in SPH

The mass density ρ plays a central role in SPH and its computation is carried out in a separate cycle during the time-stepping of the algorithm. In SPH, each of the continuous MHD fields is known only at the positions of the particles $\mathbf{r} = \mathbf{r}_a$ with -a- the particle's numbering index. In the case of the mass density the smoothing approximation means that the masses of the particles are not Dirac δ-functions centered at $\mathbf{r}_a$, but rather spread out *around* it. The spreading is not homogeneous, but concentrated at $\mathbf{r}_a$. This radial dependence is given by the weight function W known as the interpolating kernel:

$$W(|\mathbf{r}-\mathbf{r}_a|, H) = \frac{C}{H^d}\mathcal{K}\left(\frac{|\mathbf{r}-\mathbf{r}_a|}{H}\right) \tag{9}$$

where C is a constant that guarantees that W is normalised to unity, d is the dimensionality of the problem, H is its support radius (i.e., W is identically equal to zero for all radial positions $r > H$), and $\mathcal{K}$ is usually chosen from a family of functions known as the Wendland Kernels[10]. We will use the 4$^{\text{th}}$ order Wendland Kernel:

$$\mathcal{K}_{\mathrm{WC4}}(q) = \begin{cases} (1-q)_+^5\left(1+5q+8q^2\right) & d=1 \\ (1-q)_+^6\left(1+5q+35q^2/3\right) & d>1 \end{cases} \tag{10}$$

where $(\cdot)_+ = \max\{0,\cdot\}$. The values of C are $\{3/2,\ 9/\pi,\ 495/32\pi\}$ for the $d = \{1,2,3\}$ cases respectively. The local mass density can then be calculated as:

$$\rho(\mathbf{r}) = \sum_{b\in\mathcal{N}(\mathbf{r})} m_b W(|\mathbf{r}-\mathbf{r}_b|, H) \tag{11}$$

Here the summation runs along all the particles b in the neighbourhood of $\mathbf{r}$ denoted by $\mathcal{N}(\mathbf{r})$. An important characteristic of Eq. 11 is that, although the mass density could also be from Eq. 1, Eq. 11 allows us to avoid the trouble of temporal integration. Other advantages of using the direct sum instead of the temporal integration have been outlined by Price[11].

C. Ideal MHD in SPH

The discretisation of Eqs. 1, 2, 3 and 4 is done in two stages. First we focus on the reduced set of equations of ideal MHD, and later we discretise the resistive/dissipative terms individually.

The ideal MHD model can be discretised via a Hamiltonian formalism that results in discrete evolution equations that conserves mass, momentum (linear and angular) and energy down to the precision of the time integrator. The formal derivation can be found in many SPH reviews[3,5]. The resulting equations are:

$$\rho_a = m n_a \quad \text{with} \quad n_a = \sum_{b\in\mathcal{N}_a} W_{ab}(H_a) \tag{12}$$

$$\frac{\mathrm{d}\mathbf{v}_a}{\mathrm{d}t} = -\sum_{b\in\mathcal{N}_a} m\left(\frac{\mathcal{S}_a}{\rho_a^2}\frac{F_{ab}(H_a)}{\Omega_a} + \frac{\mathcal{S}_b}{\rho_b^2}\frac{F_{ab}(H_b)}{\Omega_b}\right)\cdot\mathbf{r}_{ab} \tag{13}$$

$$\frac{\mathrm{d}\mathbf{B}_a}{\mathrm{d}t} = -\sum_{b\in\mathcal{N}_a}\left(\mathbf{B}_a\otimes\mathbf{v}_{ab} - \mathbf{v}_{ab}\otimes\mathbf{B}_a\right)\cdot\frac{\mathbf{r}_{ab}}{n_b}\frac{F_{ab}(H_a)}{\Omega_a} \tag{14}$$

$$\frac{\mathrm{d}u}{\mathrm{d}t} = -\sum_{b\in\mathcal{N}_a} m\frac{p_a}{\rho_a^2}(\mathbf{v}_{ab}\cdot\mathbf{r}_{ab})\frac{F_{ab}(H_a)}{\Omega_a} \tag{15}$$

where m is the mass of each particle (which will be the same for every particle) and $\mathbf{r}_a$, n_a, ρ_a, p_a, $\mathbf{v}_a$, $\mathbf{B}_a$ and u_a corresponds to the values of the position, particle-density, mass-density, pressure, velocity, magnetic field and internal energy of the a-th particle. Also, the following notation is usually adopted in the SPH literature:

$$\mathcal{N}_a = \mathcal{N}(\mathbf{r}_a) \tag{16}$$
$$\mathbf{r}_{ab} = \mathbf{r}_a - \mathbf{r}_b \tag{17}$$
$$\mathbf{v}_{ab} = \mathbf{v}_a - \mathbf{v}_b \tag{18}$$
$$W_{ab}(H_a) = W(|\mathbf{r}_a - \mathbf{r}_b|, H_a) \tag{19}$$
$$F_{ab}(H_a) = F(|\mathbf{r}_a - \mathbf{r}_b|, H_a) \tag{20}$$

with F and W related via:

$$\nabla W_{ab}(H_a) = -\mathbf{r}_{ab}F_{ab}(H_a) \tag{21}$$

where the minus sign ensures that F is positive. The support radius H of both W and F has a spatial dependence that changes in time to ensure that the following relation always holds:

$$\mathcal{V}_d\cdot\rho_a\cdot H_a^d = m\cdot N_{\text{neighbours}} \tag{22}$$

for every particle a. Here, d is the dimensionality of the problem, $\mathcal{V}_d$ is the volume of a d-dimensional unit sphere, and $N_{\text{neighbours}}$ is a user-provided parameter that determines the number of neighbours that each particle interacts with. Finally, Ω is a correction factor that arises[3] from the fact that the support radius H is adaptable and changes in time and space. It appears in Eqs. 13, 14 and 15, and it is defined as:

$$\Omega_a = 1 + \frac{H_a}{dn_a}\sum_{b\in\mathcal{N}_a}\frac{\partial W_{ab}(H_a)}{\partial H} \tag{23}$$

D. Resistive MHD in SPH

Non-ideal effects such as resistivity cannot be included in the Lagrangian formalism and their discretisation must thus be constructed *a posteriori*. We follow Tsukamoto[9] in this regard, allowing for a spatial dependence of the resistivity field $\eta(\mathbf{r})$:

$$\left.\frac{\mathrm{d}\mathbf{B}_a}{\mathrm{d}t}\right|_\eta = n_a\sum_{b\in\mathcal{N}_a}\left(\frac{\mathcal{F}_a}{n_a^2}\frac{F_{ab}(H_a)}{\Omega_a} + \frac{\mathcal{F}_b}{n_b^2}\frac{F_{ab}(H_b)}{\Omega_b}\right)\cdot\mathbf{r}_{ab} \tag{24}$$

where the components of the tensor $\mathcal{F}$ are given by:

$$\mathcal{F}_a^{ij} = \eta_a\left[\frac{\partial B_a^j}{\partial x^i} - \frac{\partial B_a^i}{\partial x^j}\right] \tag{25}$$

The Ohmic heating term in the evolution equation of the thermal energy can then be replaced by:

$$\left.\frac{\mathrm{d}u_a}{\mathrm{d}t}\right|_\eta = -\frac{\mathbf{B}_a}{\rho_a}\cdot\left.\frac{\mathrm{d}\mathbf{B}_a}{\mathrm{d}t}\right|_\eta \tag{26}$$

E. Divergence of the Magnetic Field

Keeping the magnetic field solenoidal is essential in SPH since evolving the magnetic field $\mathbf{B}$ does *not* guarantee that it will remain solenoidal in time. Two different measures are implemented. First, a dedicated divergence-cleaning algorithm[12] is adopted to keep the magnetic divergence sufficiently small with minimum effects on $\mathbf{B}$. Secondly, a correction term[6,13] is included to avoid the spurious force[14] parallel to $\mathbf{B}$ and proportional to $\nabla\cdot\mathbf{B}$ that arises from using the discrete form of $\nabla\cdot\mathcal{S}$ instead of $-\nabla p + \mathbf{J}\times\mathbf{B}$ in the momentum equation. These correction terms are:

$$\left.\frac{\mathrm{d}\mathbf{v}}{\mathrm{d}t}\right|_{\text{divB}} = \mathbf{B}_a\sum_{b\in\mathcal{N}_a} m\left[\frac{\mathbf{B}_a}{\rho_a^2}\frac{F_{ab}(H_a)}{\Omega_a} + \frac{\mathbf{B}_b}{\rho_b^2}\frac{F_{ab}(H_b)}{\Omega_b}\right]\cdot\mathbf{r}_{ab} \tag{27}$$

$$\left.\frac{\mathrm{d}\mathbf{B}_a}{\mathrm{d}t}\right|_\phi = \sum_{b\in\mathcal{N}_a} n_a\left[\frac{\phi_a}{\Omega_a n_a^2}F_{ab}(H_a) + \frac{\phi_b}{\Omega_b n_b^2}F_{ab}(H_b)\right]\mathbf{r}_{ab} \tag{28}$$

$$\frac{\mathrm{d}\phi_a}{\mathrm{d}t} = -\frac{c_h^2}{c_p^2}\phi_a - c_h^2\sum_{b\in\mathcal{N}_a} m\ (\mathbf{B}_{ab}\cdot\mathbf{r}_{ab})\frac{F_{ab}(H_a)}{\Omega_a\rho_a} \tag{29}$$

where a new field ϕ needs to be included as a variable and time evolved. According to Tricco[12], the optimal values for c_h and c_p are $\sqrt{v_s^2+v_A^2}$ and H/σ, where v_s is the sound speed of the system, v_A is the Alfven speed, and σ is $\{0.1,\ 0.3,\ 0.5\}$ for the 1, 2 and 3-dimensional cases respectively.

In summary, Eqs. 12, 13, 14, 15, 24, 26, 27, 28 and 29 provide the full set of equations that will be used throughout this article to carry out SPH simulations within the resistive MHD model.

III. USING SPH WITH MAGNETICALLY CONFINED PLASMAS

As mentioned in Sec. I, there are three main challenges that must be addressed in order to use SPH to simulate MCPs in the context of the laboratory plasmas that we want to simulate. The solutions that we propose to each of them are summarised next.

A. Setting up arbitrary initial Conditions

The capability of starting SPH simulations with good initial conditions with low particle noise are crucial in the study of the MHD equilibrium and stability properties of MCP confined in the laboratory. The complex and convoluted geometries of plasmas confined in a tokamak and stellarator, and the fact that the density can vary by several orders of magnitudes between center and edge, make

the problem particularly delicate. In SPH the density at a given point in space is a direct consequence of the masses and the distances to the neighbouring particles (see Eq. 11). Therefore, constructing an initial condition to mimic a desired target density profile $\rho_{\rm target}(\mathbf{r})$ becomes an inverse problem where the proper masses and positions of the neighbours have to be found. The solution of this inverse problem is far from trivial and many approaches have been proposed that, in one way or another, attempt to solve it. Some of these solutions take advantage of any existing symmetries in $\rho_{\rm target}(\mathbf{r})$ to analytically place the particles, others use a low Reynolds number approximation of the momentum equation that eliminates the inertial effects from the particle motions, or assign different masses to every particle so for a given set of particle positions the masses will directly define the density, or even use external potentials to relax the particles onto the desired profile.

In our case, we have proposed a new algorithm known as ALARIC, an acronym for ALgorithm to construct ARbitrary Initial Conditions. Details of the algorithm can be found elsewhere[7]. It suffices to say here that ALARIC provides very low-noise, high quality solutions to the inverse problem in a relatively short amount of time for geometries as complicated as the ones of interest in the context of magnetically confined fusion plasmas. It uses a particular combination of relaxation techniques, high viscosity and friction, recurrent nullification of the velocities in the system and particle-splitting events that, altogether combine the flexibility of the relaxation methods with the superior convergence speed of the inertia-free methods and delivers results with very low levels of particle noise.

B. Treatment of smoothly Curved Boundaries

In SPH boundary conditions are usually enforced by means of ghost particles. This approach is rather straightforward and very efficient at avoiding particle penetration in or out-of the domain. However, whenever curved or jagged boundaries are present, the usual approach of placing the ghost particle at the reflected positions with respect to the local tangent plane, the so-called mirror-positioning, fails. It will produce spurious accumulation/depletion of ghost particle mass in the case of curved walls, or will require to place ghost particles back into the computational domain in some pathological cases with zig-zag boundaries. This is certainly the case of a fusion plasma confined in a tokamak or stellarator, where boundary conditions must be enforced on toroidal surfaces that can become extremely complicated. Our solution to this challenging problem has been to develop a generalised version of the "*mirror with respect to the local tangent plane*"-principle for smoothly curved boundaries[8]. A generalised positioning map, Ψ, is introduced that will determine the exact position of the ghost particle taking into account the local curvature(s) of the boundary. The map Ψ can be obtained once a specific set of local coordinates $\{s, u, v\}$ (with Jacobian $\mathcal{J}$) is available that fulfils the following requirements:

1.) The boundary of interest corresponds to the $s = 0$ surface ($s < 0$ for the inside of the domain and $s > 0$ for the outside.)

2.) The shortest path joining the internal particle (for which a ghost particle is needed) with the boundary is given by the intersection of the surfaces $u = u_0$ and $v = v_0$, being u_0 and v_0 two constants.

In this system of coordinates, the positioning map Ψ will determine the position of the ghost particle, given the position of the internal particle, as:

$$\begin{pmatrix} s_{a'} \\ u_{a'} \\ v_{a'} \end{pmatrix} = \mathbf{r}_{a'} = \Psi(\mathbf{r}_a) = \begin{pmatrix} \psi(s_a) \\ u_a \\ v_a \end{pmatrix} \tag{30}$$

It should be noted that, in the local coordinates, both the inner particle and the reflected ghost particle share the same u and v coordinates, while the s-coordinate is specified via the function ψ that can be found by solving the following differential equation:

$$\frac{\partial \psi(s,u,v)}{\partial s} = -\frac{\mathcal{J}(s,u,v)}{\mathcal{J}(\psi(s),u,v)} \tag{31}$$

with the boundary condition $\psi(0) = 0$. The function ψ (and therefore the map Ψ) can be found analytically, for simple 3D geometries, or numerically for arbitrary 2D and 3D shapes. Among the interesting shapes for which Ψ can be found analytically[8], straight cylinders are of particular interest to us since several nonlinear MHD simulations of plasma cylindrical pinches will be used in later sections to illustrate the performance of our implementation.

C. Boundary Conditions for the Magnetic Field

One of the novelties of this paper resides in that, once the solution for the allocation of ghost particles that we described in the previous section is available, the answer to the unavoidable question of how to enforce boundary conditions for MCPs for various fields becomes much more transparent. According to the ideal MHD set of equations, the total energy of the system will be conserved unless some of it flows through the boundary:

$$\frac{\partial E}{\partial t} = -\oint_{\partial\Omega} \left[\left(\frac{\rho v^2}{2} + \gamma \rho u + \frac{B^2}{\mu_0} \right) (\mathbf{v}\cdot\hat{\mathbf{n}}) - \frac{(\mathbf{B}\cdot\mathbf{v})}{\mu_0} (\mathbf{B}\cdot\hat{\mathbf{n}}) \right] \mathrm{d}S \tag{32}$$

that evidently is equal to zero when the velocity and the magnetic field satisfy the following boundary conditions:

$$\mathbf{v}\cdot\hat{\mathbf{n}}=0 \qquad \text{and} \qquad \mathbf{B}\cdot\hat{\mathbf{n}}=0 \tag{33}$$

The boundary condition on the velocity vector can then be easily implemented at each ghost-particles by assuming that they reflect the normal component with respect to the local tangent plane, and leave the tangential component unchanged (Free-Slip condition) or reverse it (No-Slip condition). This is usually achieved by assigning to the velocity field of the ghost particle the following values:

$$\mathbf{v}_{a'}=\left(-\hat{\mathbf{n}}\hat{\mathbf{n}}\pm\hat{\mathbf{t}}\hat{\mathbf{t}}\pm\hat{\mathbf{s}}\hat{\mathbf{s}}\right)\cdot\mathbf{v}_a \tag{34}$$

where the orthonormal triad $(\hat{\mathbf{n}},\hat{\mathbf{t}},\hat{\mathbf{s}})$ constitutes an appropriate coordinate system (The vector $\hat{\mathbf{n}}$ is normal to the surface $\partial\Omega$, while the pair $(\hat{\mathbf{t}},\hat{\mathbf{s}})$ span a plane tangential to $\partial\Omega$), the symbol $\hat{\mathbf{n}}\hat{\mathbf{n}}$ corresponds to the dyad $\hat{\mathbf{n}}\otimes\hat{\mathbf{n}}$ and the $\pm$ signs reflects the free-slip/no-slip choice respectively.

If one assumes that the boundary corresponds to either a magnetic surface or a perfect conductor, the natural condition for the magnetic field would be $\mathbf{B}\cdot\hat{\mathbf{n}}=0$, suggesting that $\mathbf{B}$ should be treated in an analogous manner to the velocity. That is, the values of $\mathbf{B}$ on the ghost particles should be given by:

$$\mathbf{B}_{a'}=\left(-\hat{\mathbf{n}}\hat{\mathbf{n}}+\hat{\mathbf{t}}\hat{\mathbf{t}}+\hat{\mathbf{s}}\hat{\mathbf{s}}\right)\cdot\mathbf{B}_a \tag{35}$$

which means that the net transport of energy in/out of the system due to magnetic effects vanishes, and the total energy of the system conserved.

IV. BENCHMARKS AND RESULTS

We will now demonstrate the performance of our SPH implementation (namely, the full set of equations described in Sec. II plus the initialization and boundary treatments described in Sec. III) while simulating three different nonlinear, resistive MHD scenarios. The particle equations are advanced in time by using a standard symplectic 2nd-order predictor-corrector integrator, with a time step selected to ensure that all relevant physical timescales are well resolved.

A. Propagation of circularly-polarized Alfvén waves

This test is rather standard in the SPH literature[15,16], being particularly useful to test the non-linear capabilities and convergence features of our SPH implementation of the MHD equations since circularly-polarized Alfven waves are analytical solutions of the MHD equation for arbitrary amplitudes. The initial condition for the plasma velocity and the magnetic field is given by:

$$\begin{pmatrix} v_\perp \\ v_\parallel \\ v_z \end{pmatrix} = \begin{pmatrix} B_\perp \\ B_\parallel \\ B_z \end{pmatrix} = \begin{pmatrix} 0.1\sin\left(2\pi x_\parallel\right) \\ 0 \\ 0.1\cos\left(2\pi x_\parallel\right) \end{pmatrix} \tag{36}$$

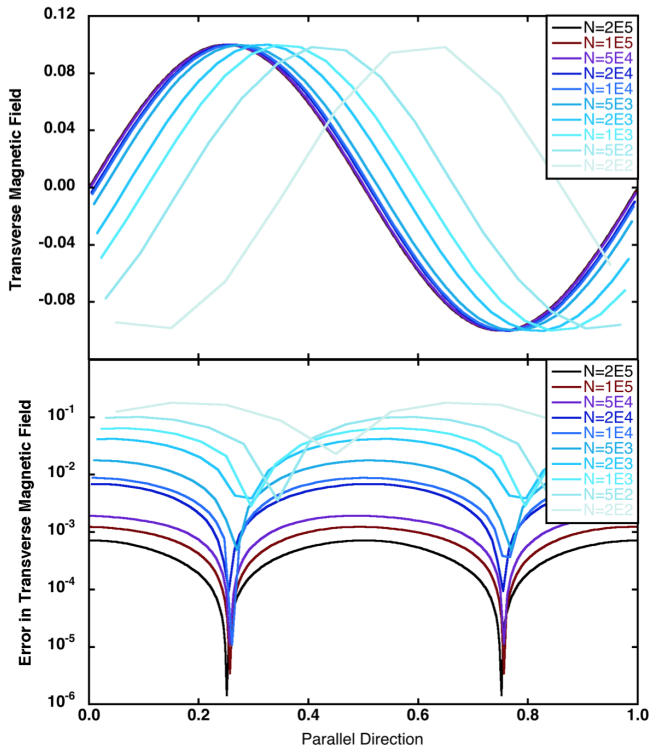

FIG. 1. Convergence of the wave front for increasing total number of particles N. The upper plot depicts the wave front after 5-crossings. The lower plot shows the absolute value of the errors in logarithmic scale.

where the parallel and perpendicular directions are:

$$\begin{pmatrix} x_\parallel \\ x_\perp \end{pmatrix} = \begin{pmatrix} \cos\alpha & \sin\alpha \\ -\sin\alpha & \cos\alpha \end{pmatrix} \begin{pmatrix} x \\ y \end{pmatrix} \tag{37}$$

The values of the remaining fields[15] are chosen so that the resulting Alfvèn speed brings the wave back to its starting position after one second. The smoothness of the problem allows to use it to establish the convergence of our method. To do so, we initialise the system with 10 different number of particles (starting at $N=200$ and increasing geometrically up to $N=200$k) arranged in an hexagonal lattice in a 2D periodic domain, and let the system evolve in time until the wave has crossed 5 times the computational domain. Fig. 1 shows the perpendicular component of the magnetic field along the $x_\parallel$-direction at $t=5.0s$. The upper plot clearly shows how the wave converges to the original wave-form, in both amplitude and phase, while the lower plot, corresponding to the absolute value of $B_\perp(t)-B_\perp(0)$, shows how the errors steadily become smaller as N is increased.

The L^1-norm of these errors, shown in Fig. 2, demonstrates that our SPH implementation offers a convergence of order ~ 1.77 in the high-resolution regime which is close to the second order convergence usually reported in other SPH codes such as ATHENA[16] or PHANTOM[6].

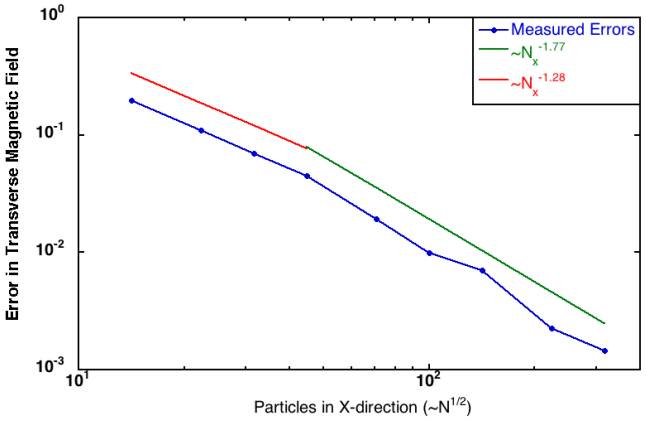

FIG. 2. Scaling of the L^1-norm of the error as a function of the approximate number of particles in the x-direction. The scaling is of order ~ 1.28 for the low-resolution scenarios, but improves to ~ 1.77 for the well-resolved regime.

B. Magnetic reconnection in the Harris current sheet

This test is used to demonstrate that our SPH implementation is also able to capture reconnection phenomena with a resistivity profile that could change in both time and space. It is worth to note that we have not been able to find similar simulations using SPH in the literature, although the SPH discretisation of the resistive term has been previously discussed in the literature[9]. The problem we consider is the evolution of a variant of the Harris current sheet test. The initial magnetic configuration is given by:

$$\begin{pmatrix} B_x \\ B_y \\ B_z \end{pmatrix} = \begin{pmatrix} 0 \\ \tanh\left[(x-x_0)/\lambda\right] \\ \cosh^{-1}\left[(x-x_0)/\lambda\right] \end{pmatrix} \tag{38}$$

where $\lambda = 0.2$ and $x_0 = 0.5$. Additionally, a spatially varying resistivity profile is included:

$$\eta(x,y) = \eta_0 \,\mathrm{sech}\left[A\sqrt{\left(x-\frac{1}{2}\right)^2 + \left(\frac{y-y_0}{4}\right)^2}\right] \tag{39}$$

The parameters $\{\eta_0, A, y_0\}$ correspond to the value of η at the centre of the resistive "hot-spot", the broadness of the source and its vertical position, respectively. The simulations used 10k particles in a hexagonal array inside the rectangular domain $(x,y) \in [0,1]\times[0,4]$ and they run for 100 Alfven times each. The domain is periodic in the x-axis and has $\mathbf{v}\cdot\hat{\mathbf{n}} = \mathbf{B}\cdot\hat{\mathbf{n}} = 0$ boundary conditions on the y-direction. Fig. 3 shows the state of four different simulations at the end of the run. Each simulation differs only in their value of $\eta_0 = \{10^{-4}, 10^{-3}, 10^{-2}, 10^{-1}\}$, but they all have the same values for $A = 32$ and $y_0 = 2$.

Fig. 4 shows the time trace of the kinetic energy of the system. In red, the time history for the case in which the

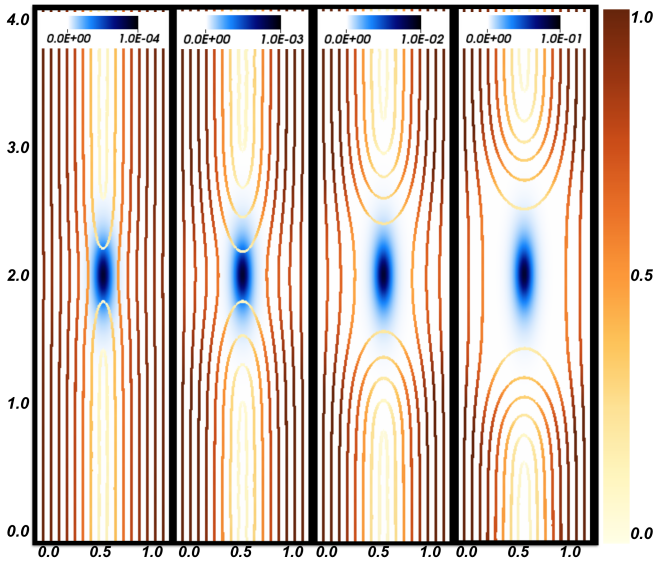

FIG. 3. Magnetic field lines (Black/Orange/Yellow) and resistivity (White/Blue/Black) at the end of 100 Alfven times for the Harris Current Sheet test. The four pictures correspond to four different values of the parameter η_0 in Eq. 39. From left to right the values correspond to $\{10^{-4}, 10^{-3}, 10^{-2}, 10^{-1}\}$.

SPH particles are initially distributed using an hexagonal crystalline lattice is shown. Three distinct regions can be identified: 1) an initial phase characterised by a peak in the kinetic energy of the system, 2) a secondary phase where the kinetic energy grows exponentially, and 3) a last phase when it saturates and the non-linear effects take over. The first growth phase can be attributed to the underlying crystalline lattice chosen to initialize the particles. Due to the presence of the lattice, any force acting on the crystal will create "dislocations" that increase the system kinetic energy and appear as a peak in its time history. The peak subsides once the the lat-

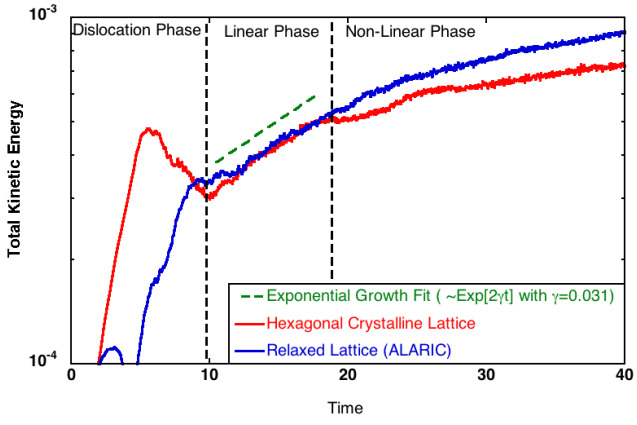

FIG. 4. Time history of the kinetic energy for the two runs of the Harris current sheet test discussed.

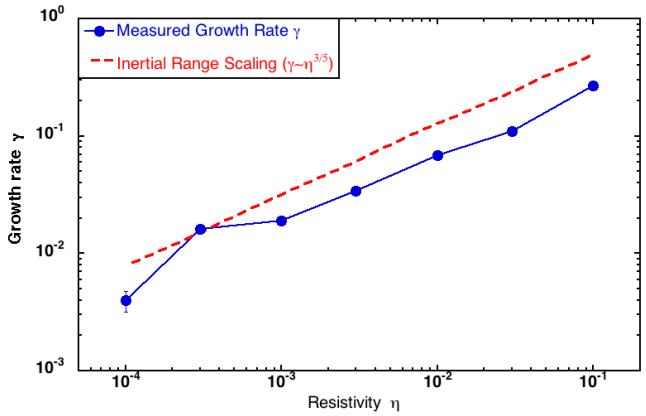

FIG. 5. Scaling obtained by comparing the growth rates of the reconnection simulation for different values of the parameter η_0. The measured values in blue scale in accordance with the $\eta^{3/5}$ behaviour predicted by the linear theory in red.

tice morphs into a glass-like structure, point at which the exponential growth predicted by the linear theory is observed for a short period until non-linear effects become dominant and the time trace seems to saturate. The "dislocation" explanation is confirmed by rerunning the same simulation but initialising the particles instead with a relaxed structure obtained with ALARIC[7]. Fig. 4 also includes (in blue) the time history of the kinetic energy of the relaxed structure, that lacks the initial peak in the kinetic energy, transiting directly to the linear growth phase of the reconnection and leading to a stronger non-linear phase as well. We have quantified the growth rate γ of the linear phase and compared with the scaling predicted by linear theory[17,18], $\gamma \propto S_L^{-3/5}$, being S_L is the Lundquist number that is in turn inversely proportional to the resistivity of the system. The scaling obtained in our runs is shown in Fig. 5 where a reference $\eta^{3/5}$ slope has been added to the graph. The good agreement with the linear theory is apparent.

C. MHD stability of cylindrical pinches

Next, we examine with our SPH implementation the MHD stability of three types of cylindrical pinches (the Theta-pinch, the Zeta-pinch and the Screw-pinch) and compare the results with those of linear theory. All pinches consider a cylindrical domain of radius $R = 1$ that extends longitudinally from $Z_{\min} = -3$ to $Z_{\max} = +3$. The z-direction has periodic boundary conditions while the walls of the cylinder are treated with the free-slip condition on $\mathbf{v}$ and $\mathbf{B}\cdot\hat{\mathbf{n}} = 0$. The divergence cleaning techniques previously described are used in all simulations.

1. Theta-pinch

The Theta-pinch considered has the following pressure and axial magnetic field radial profiles:

$$\frac{p(r)}{p_0} = 1 - \left[1 - \beta\left(1 - r^2\right)^2\right]^2 \tag{40}$$

$$\frac{B_z(r)}{B_0} = 1 - \beta\left(1 - r^2\right)^2 \tag{41}$$

The parameter β is given by:

$$\beta = \frac{\beta_0}{1 + \sqrt{1 - \beta_0}} \qquad \text{and} \qquad \beta_0 = \frac{2p_0}{B_0} \tag{42}$$

where p_0 and B_0 are the values of the pressure, and the azimuthal magnetic field at the magnetic axis. For our simulation we have considered the values $p_0 = 1$ and $B_0 = 2$ which leads to $\beta_0 = 0.5$. Linear theory predicts[19] that, once in equilibrium, the Theta-pinch will be stable against any kind of perturbation. Our runs are consistent with this result as we discuss next.

We have run ALARIC to obtain an scenario for the Theta-pinch with 50K particles with a flat density inside a cylinder of radius $R = 1$ and length $L_z = 6$. The velocities of the system were randomly initialized and then rescaled to ensure that the total kinetic energy of the system at $t = 0$ is exactly $E_k(0) = 10^{-6}$. Fig. 6 shows the values of the pressure field in the y-axis represented against the radial position of each particle. Since the profiles of the Theta-pinch are independent of the angle θ or the coordinate z, all values fall into a well-defined curve. We can see how the sum of the two (in green), that is, the

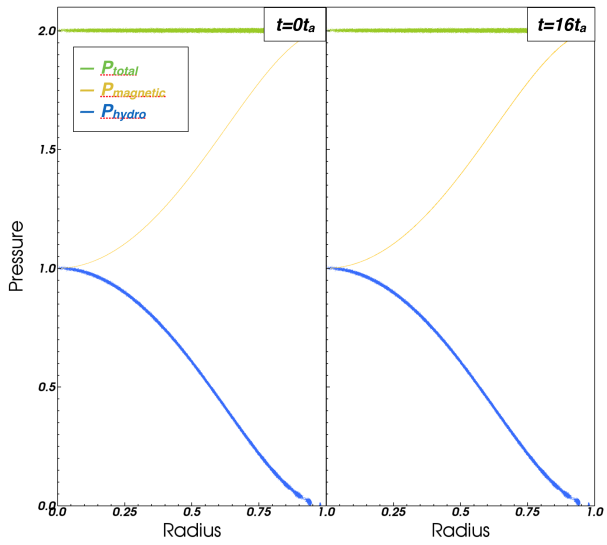

FIG. 6. Initial and final values for the pressure field plotted against the radial coordinate of each particle. Each panel depicts the radial dependence of the hydrodynamic (Blue), the magnetic (Yellow) and the total pressure (Green).

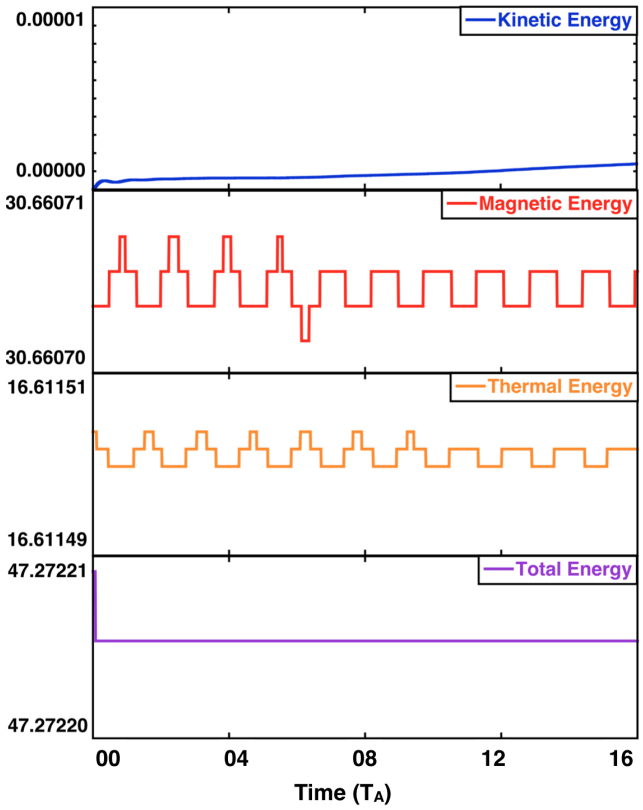

FIG. 7. Time histories of the kinetic, magnetic, thermal and total energy in the system.

total pressure of the system, is flat which automatically fulfils the equilibrium condition for the Theta-pinche[19].

The right panel of Fig. 6 shows the radial profiles after the simulation have been run for 16 Alfvèn times using 50K particles. Clearly, the profiles do not exhibit any noticeable change as should be expected in a stable system. Additionally, Fig. 7 shows the time trace of the different contributions of the energy in the system. No noticeable linear growth rate is present in the system except for a slight increment observed in the kinetic energy, that can be attributed to numerical particle noise and that holds no statistical significance. Indeed, the associated growth rate, that is roughly $\gamma \approx 0.029\ s^{-1}$ for 50K particles, reduces to $\gamma \approx -0.004\ s^{-1}$ for 500K particles.

2. Zeta-pinch

For the Zeta-pinch we proceed in a similar manner. We have initialised the plasma profiles according to:

$$\frac{p(r)}{p_0} = \frac{1}{(1+r^2)^{\nu}} \tag{43}$$

$$\frac{B_\theta^2(r)}{B_0^2} = \frac{1}{1-\nu}\frac{1}{r^2}\left[1 - \frac{1+\nu r^2}{(1+r^2)^{\nu}}\right] \tag{44}$$

where we have chosen $p_0 = 1.0$, $B_0 = \sqrt{2}$ and $\nu = 2.5$. These profiles fulfil the Zeta-pinch condition for equilibrium[19]. The linear-stability theory for the Zeta-pinch predicts that any equilibrium whose Kadomtsev functions becomes negative in any radial interval can become unstable. The Kadomtsev function is given by:

$$K_m(r) = \begin{cases} \frac{2\gamma B_\theta^2}{B_\theta^2+\gamma p} + r\frac{p'}{p} & \text{for } m = 0 \\ \\ rp' + \frac{m^2 B_\theta^2}{2} & \text{for } m \geq 1 \end{cases} \tag{45}$$

where m is the poloidal wavenumber. The Kadomtsev functions that correspond to the selected profiles (that is, Eqs. 43 and 44) are shown in Fig. 8 for different values of m. Clearly, modes with $m \geq 2$ are stable but modes $m = 0$ and $m = 1$ can be excited since they are negative in the whole radial domain.

The evolution of the pressure field obtained by our SPH implementation is displayed in the four panels of Fig. 9. It is apparent that the radial profiles broaden to a point of complete distortion due to the fact that they become strongly dependent on the θ and z coordinates and therefore, when projected onto the radial coordinate, no longer lie on top of a well-defined curve.

Fig. 10 shows iso-surfaces of the hydrodynamical pressure at the same temporal instants where the radial profiles were shown in Fig. 9. From it, it is clear that a kink-type instability sets on around $t = 12t_c$, where t_c is the crossing time of the system defined as $t_c = L_{\rm char}/c_s$ with $L_{\rm char}$ a characteristic length of the system, in this case the radius of the cylindrical domain, and c_s the speed of sound. The dominant instability is identified to be an $m = 1$ (kink) with azimuthal wave number $4 < k < 5$. The Fourier analysis of the pressure perturbation field $\delta P(\mathbf{r}, t) = P(\mathbf{r}, t) - P(\mathbf{r}, 0)$ at exactly $t = 12t_c$ corroborates this. We have selected the values of the perturbed

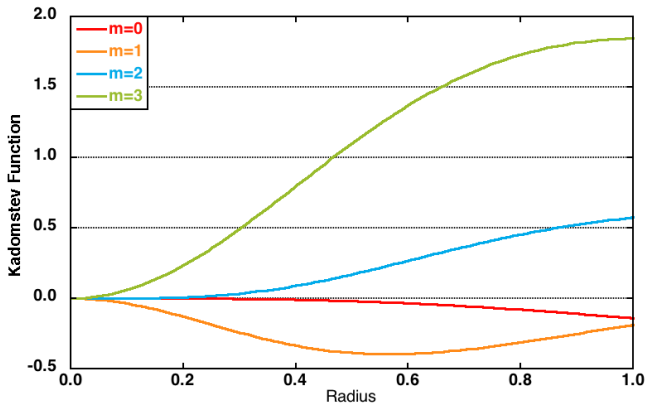

FIG. 8. Kadomtsev function for different values of the poloidal wavenumber m. For the profiles used, the profiles are unstable against the $m = 0$ and $m = 1$ modes and stable for all modes $m \geq 2$.

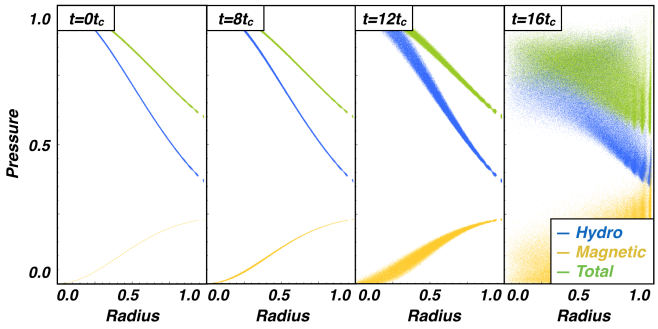

FIG. 9. Initial and final values of the pressure field projected onto the radial component. Each panel depicts the radial dependence of the hydrodynamic (Blue), the magnetic (Yellow) and the total pressure (Green).

pressure on the cylindrical shell at $r = 0.5$. The resulting δP at $t = 12t_c$ is depicted on the left panel of Fig. 11, while its Fourier transform is shown on the right panel. It is apparent that the mode $(m, k) = (1, 5)$ indeed dominates, with smaller non-zero contributions from the modes $(m, k) = (1, 4)$ and $(m, k) = (-1, 5)$.

It is also possible to obtain a semi-analytical estimation of the growth rate of any specific mode via a normal-mode analysis[19]. The result of inserting the radial profiles from Eqs. 43 and 44 and considering a mode with $m = 1$ and $k = 5$ in this estimate yields a theoretical prediction for the growth rate equal to $\gamma_{\text{Normal-Mode}} = 1.1802\ s^{-1}$. On the other hand, one can also measure the growth rate directly from the time trace of the kinetic energy of the Zeta-pinch, shown in Fig. 12. Keeping in mind that the growth of the kinetic energy is twice that of the real growth of the perturbation we obtain $\gamma_{\text{perturbation}} = \gamma_{\text{energy}}/2 = 0.961\ s^{-1}$. Therefore, there is a difference of about 18% for the 50K particle case. This is not too bad considering that our SPH implementation is not doing a linear analysis of an isolated mode but carries out instead a full nonlinear evolution of the MHD equations where many unstable modes coexist, nonlinearly transferring energy among them.

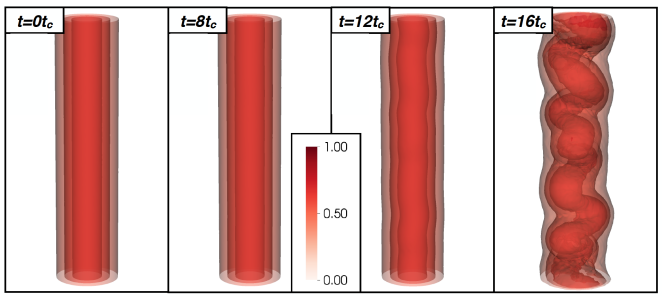

FIG. 10. Isosurfaces of the hydrodynamic pressure field at the same temporal instants as Fig. 9.

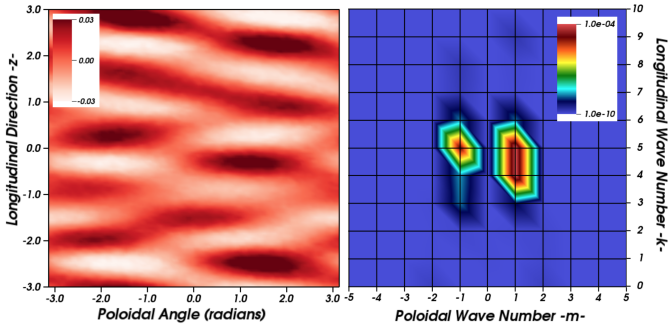

FIG. 11. Perturbation pressure field $\delta P = P - P(0)$ at $t = 12t_c$ over the cylindrical shell $r = 0.5$ (Left). Fourier transform of the image show in the left panel (Right).

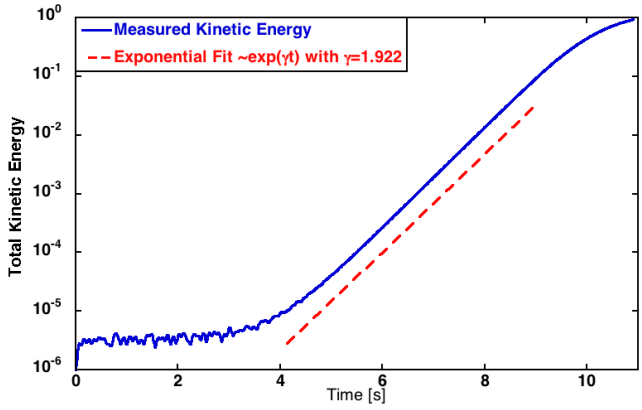

FIG. 12. Time history (in blue) of the kinetic energy of the Zeta-pinch in semi-log scale. The best exponential fit to the linear growth phase is shown in dashed red.

3. Screw-pinch

Our last cylindrical MHD simulation corresponds to the Screw-pinch. The specific profiles used in this test are:

$$\frac{p(r)}{p_0} = (1 - r^2)^2 \left[1 + 2r^2 - r^4 + \frac{2}{3}\left(\frac{\varepsilon}{q^\star}\right)^2 (5 - 2r^2)\right] \tag{46}$$

$$\frac{B_z(r)}{B_0} = r^2(2 - r^2) \tag{47}$$

$$\frac{B_\theta(r)}{B_0} = r\left(\frac{\varepsilon}{q^\star}\right)(2 - r^2) \tag{48}$$

Here, the symbol ε is a measure of the aspect ratio of the column, defined as the ratio between its "minor" and "major" radius, the first one corresponding to the cylinders radius, and the second to an effective value R_0 such

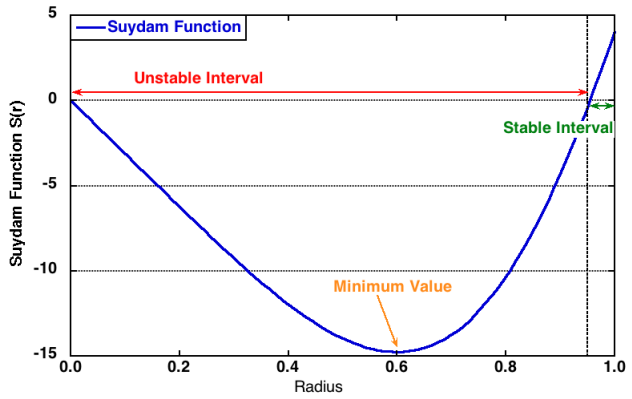

FIG. 13. Suydam function for the Screw-pinch calculated using the selected profiles (Eqs. 46, 47 and 48).

that $2\pi R_0 = Lz = 6$). In our case this yields $\varepsilon = \pi/3$. The parameter $q^\star$ is defined as the rotational transform at the outermost radial position, that is:

$$q(r) = \frac{r}{R_0}\frac{B_z(r)}{B\theta(r)} = \frac{r^2}{R_0}\frac{q^\star}{\varepsilon} = r^2 q^\star \qquad (49)$$

which implies $q(r = 1) = q^\star$. Finally, we have used the values $B_0 = 1$ and $p_0 = 0.5$. Also, as in the cases of the Zeta and Theta pinches, we have initialized the system with an homogeneous mass density profile $\rho(r) = \rho_0$ using 50K particles and simply assigned to the thermal energy $u(r)$ the necessary radial dependence to give rise to the required pressure profile.

Linear-stability analysis[19] predicts that if Suydam's function $S(r)$ were to have any negative values, then a perturbation could be constructed such that it could destabilise the system. Suydam's function is given by:

$$S(r) = rB_z^2\left(\frac{q'}{q}\right)^2 + 8p' \qquad (50)$$

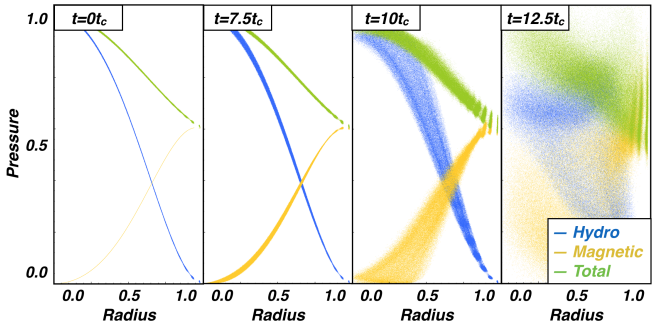

FIG. 14. Radial pressure profiles at simulation times $t = \{0, 7.5, 10, 12.5\}t_c$. Each panel depicts the radial dependence of the hydrodynamic (Blue), the magnetic (Yellow) and the total pressure (Green).

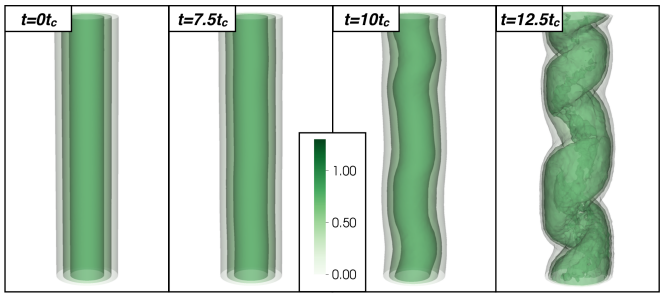

FIG. 15. Isosurfaces of the hydrodynamic pressure field at the same temporal instants shown in Fig 14.

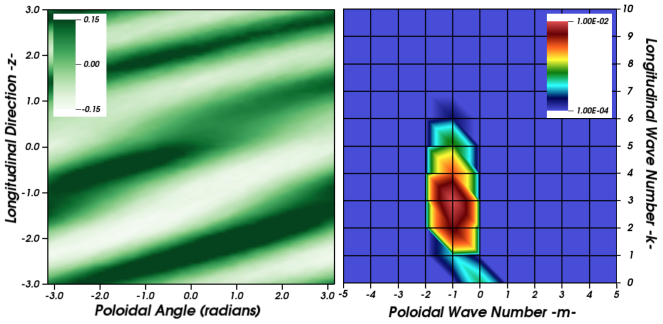

FIG. 16. Value of the perturbation pressure field $\delta P = P - P(0)$ at $t = 10t_c$ over the cylindrical shell $r = 0.5$ (Left). Fourier transform of the image show in the left panel (Right).

For our particular choice of radial profiles, the value of Suydam's function is depicted in Fig. 13. We can see that $S(r)$ is negative along most of the radial domain (negative for $0 < r < 0.95$) and positive only at the edge $0.95 < r < 1$. Therefore, a perturbation which happens to be localised along the unstable interval could potentially destabilise the system.

The Screw-pinch has been evolved for 16 crossing times. Fig. 14 shows the initial radial profiles and their snapshots at the selected times $t = \{0, 7.5, 10, 12.5\}t_c$. We can also see in Fig. 15 that, as in the case of the Zeta-pinch, a kink-like perturbation appears to be excited. In particular, the last panel ($t = 12.5t_c$) shows that the dominant mode has a k-number in the range $2 < k < 3$. To isolate the dominant perturbation, we proceed as with the Zeta-pinch. The left panel in Fig. 16 shows the values of the perturbation pressure field δP over the cylindrical shell $r = 0.5$ at time $t = 10t_c$, while the right panel shows its Fourier transform. Clearly, the main contribution comes from the mode $(m, k) = (-1, 3)$ with smaller contributions from the $(m, k) = (-1, 2)$ mode.

Normal-mode analysis[19] predicts now a value for the growth rate of the dominant $(m, k) = (-1, 3)$ mode equal to $\gamma_{\text{Normal-Mode}} = 0.586\ s^{-1}$, whilst the direct measurement from the kinetic energy time trace yields $\gamma_{\text{perturbation}} = \gamma_{\text{energy}}/2 = 0.461\ s^{-1}$. That is, a difference of about 21% for the 50K particle case. In this case, we have tested the convergence of the result by re-

running a case with 500K particles. The dominant mode of the higher-resolution run comes to be still the one with $(m, k) = (-1, 3)$, as shown in Fig.18, and the growth rate obtained is $\gamma_{\text{perturbation}} = 0.51\ s^{-1}$ which differs from the linear estimate in just a 13%. This difference is not so meaningful due to the same arguments made in the case of the Zeta-pinch, but the fact the the dominant mode remains unchanged when the resolution is increased by a ten-fold hints at a well-converged result.

V. CONCLUSIONS AND FUTURE WORK

In this paper we have demonstrated that SPH is a powerful formalism that can be extended and adapted to simulate MHD scenarios not just for astrophysical plasmas, but also of interest for magnetically confined fusion plasmas. Among other things, the application to fusion problems has required the introduction of a novel proper treatment of boundaries and boundary conditions and a more powerful, low-particle-noise initialization of profiles. Both proposals have been tested successfully in this paper on a variety of test problems that include Alfvèn wave propagation, magnetic reconnection and the MHD stability properties of cylindrical pinches.

There is still a significant amount of work that must be completed before our SPH implementation can be applied to actual toroidal plasmas such as those confined in tokamaks or stellarators. We are however happy to report that dealing with the realistic toroidal geometries typical of these devices will not represent a qualitative obstacle since SPH works in Cartesian coordinates and the numerical remapping methods described in this paper will easily be able to position ghost particles across toroidal boundaries. Probably, the area where we can expect the largest amount of work in the near future is the efficient parallelization of the code. Since all information is carried by particles in SPH, there is no need for domain-decomposition techniques. But a very efficient parallelization of the neighbour-search algorithms is critical. In this regard, we expect to benefit from the large body of knowledge that exists in other areas such as the molecular dynamics or numerical optimization communities.

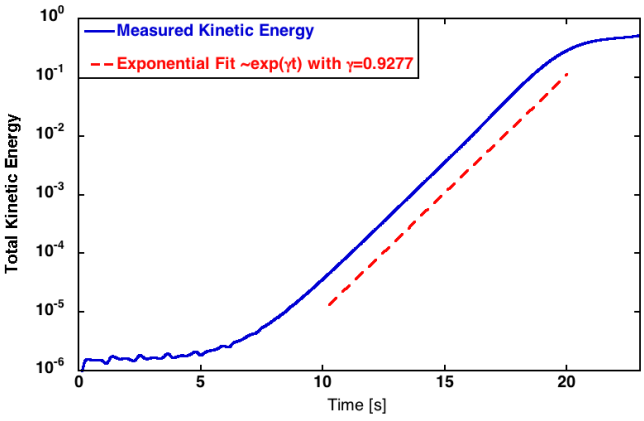

FIG. 17. Measured Kinetic Energy for the Screw-pinch for the 50K particle simulation.

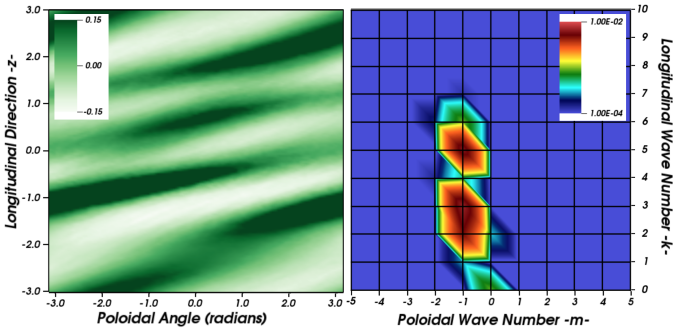

FIG. 18. Fourier transform of the perturbation pressure field $\delta P = P - P(0)$ over the cylindrical shell $r = 0.5$ during the exponential growth phase for the 500K particle run.

ACKNOWLEDGEMENTS

This research was sponsored by DGICYT (Dirección General de Investigación Científica y Técnica) Project No. ENE2015-68265, MINECO (Ministerio de Economía y Competitividad) Project No. UNC313-4E-2361, and the Erasmus Mundus Program: International Doctoral College in Fusion Science and Engineering FUSION-DC.

BIBLIOGRAPHY

[1]Gingold, R. A., & Monaghan, J. J. 1977, Mon. Notices Royal Astron. Soc., 181, 375
[2]Lucy, L. B. 1977, Astron. J., 82, 1013
[3]Price, D. J. 2012, J. Comput. Phys., 231, 759
[4]Steinmetz, M., & Mueller, E. 1993, Astron. Astrophys., 268, 391
[5]Monaghan, J. J. 2005, Rep. Prog. Phys., 68, 1703
[6]Price, D.J. 2017, Publ. Astron. Soc. Aust., 35, e031
[7]Vela L.E. 2017, Comput. Phys. Commun., 224, 186
[8]Vela L.E. 2018, (submitted to) J. Comput. Appl. Math.
[9]Tsukamoto Y., Iwasaki K., & Inutsuka S. 2013, Mon. Notices Royal Astron. Soc., 434, 2593
[10]Dehnen, W., & Aly, H. 2012, Mon. Notices Royal Astron. Soc., 425, 1068
[11]Price, D. J. 2008, J. Comput. Phys., 227, 10040
[12]Tricco, T. S., & Price, D. J. 2012, J. Comput. Phys., 231, 7214
[13]Børve, S., Omang, M., & Trulsen, J. 2004, Astrophys. J., 153, 447
[14]Brackbill, J.U., & Barnes, D.C. 1980, J. Comput. Phys., 35, 426
[15]Tóth, G. 2000, J. Comput. Phys., 161, 605
[16]Stone, J. M., Gardiner, T. A., Teuben, P., Hawley, J. F., & Simon J. B,. 2008, Astrophys. J., 178, 137
[17]Furth, H. P., Killeen, J., & Rosenbluth, M. N. 1963, Phys. Fluids, 6, 459
[18]Chacón, L., Knoll, D. A., & Finn, J. M. 2002, J. Comput. Phys., 178, 15
[19]Freidberg, J. P., *Ideal MHD*, 2014, Cambridge University Press